Additive Manufacturing 110 (2025) 104950

Contents lists available at ScienceDirect

Additive Manufacturing

journal homepage: www.elsevier.com/locate/addma

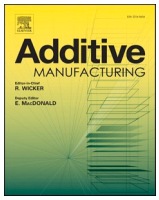

Phase-separation-driven cracking in additive manufacturing of Ni-Cu alloy systems

Andaç Özsoy [a,b], Steve Gaudez [a], William A. Hearn [a], Antonios Baganis [c,d], Zoltán Hegedüs [e], Yunhui Chen [f,g], Alexander Rack [f], Roland E. Logé [b], Steven Van Petegem [a,*]

[a] Laboratory for Condensed Matter, PSI Center for Photon Science, Villigen, Switzerland
[b] Laboratory of Thermomechanical Metallurgy (LMTM), École Polytechnique Fédérale de Lausanne (EPFL), Neuchatel, Switzerland
[c] Empa, Swiss Federal Laboratories for Materials Science and Technology, Dübendorf, Switzerland
[d] Laboratory for Photonic Materials and Characterization, École Polytechnique Fédérale de Lausanne (EPFL), Lausanne, Switzerland
[e] Deutsches Elektronen-Synchrotron (DESY), Hamburg, Germany
[f] ESRF — The European Synchrotron, Grenoble, France
[g] RMIT Centre for Additive Manufacturing, RMIT University, Melbourne, Australia

ARTICLE INFO

Keywords:
Additive manufacturing
Solidification cracking
Immiscibility
Multi-material
operando X-ray

ABSTRACT

This study investigates the cracking mechanism in additive manufacturing of Ni-Cu multi-material combinations using *operando* X-ray diffraction and imaging experiments during laser powder-bed fusion (L-PBF) of CuCrZr and IN625. It is shown that liquid immiscibility between the two alloy systems stems from the interaction between Cu and the alloying elements in IN625, causing both Cu-rich and Ni-rich liquids to form with different freezing ranges. Consequently, solidification cracking takes place due to the large solidification range where the Ni-rich solid and Cu-rich liquid co-exist. Guided by thermodynamic calculations, it was identified that the highest crack susceptibility occurs between 20 and 40 wt% CuCrZr-IN625, which was further validated by printing mixtures of the two alloys in different ratios. *Operando* X-ray imaging and scanning electron microscopy characterization revealed that the cracking occurred during the terminal stage of solidification. It was observed that the columnar grains of the Ni-rich primary solid separate into cracks, where Cu-rich liquid regions persist over a wide temperature range as the solidification of these regions begin significantly later. It was concluded that the mechanism of cracking explained in this study could be extended to other Cu-Ni alloy combinations containing elements that induce immiscibility when mixed with Cu during fusion-based processing methods.

1. Introduction

Copper and copper alloys are key materials for technological development due to their excellent thermal and electrical conductivity. They are used in a wide range of applications, including electronics, heat exchangers, medical devices, and marine impellers. Similarly, nickel-based alloys are important materials for technological development and are used in industries such as aerospace, energy, marine, and automotive where high-temperature strength and corrosion resistance are crucial. Manufacturing multi-material parts using copper and nickel-based alloys is therefore an attractive option for applications that require both properties such as heat exchangers and liquid-propellant rocket engines [1–3].

To produce parts with intricate shapes and material transitions, additive manufacturing (AM) methods, especially laser powder-bed fusion (L-PBF) and laser directed energy deposition (L-DED), provide unique capabilities. These techniques enable precise control over both the material feedstock and process conditions, capabilities that are generally limited in conventional manufacturing methods. However, the printability of a given multi-alloy combination using AM depends on a set of challenges dictated by the metallurgical behavior of the alloy systems and the processing conditions. Therefore, in addition to having been investigated via conventional methods such as casting [4–6], welding [7] and brazing [8] in the past, copper-nickel alloy combinations have recently been of interest for AM applications.

Table 1 provides a summary on the processing Cu and Ni alloy

* Corresponding author at: Paul Scherrer Institute, Forschungsstrasse 111, Villigen PSI 5232, Switzerland.
E-mail address: steven.vanpetegem@psi.ch (S. Van Petegem).

https://doi.org/10.1016/j.addma.2025.104950
Received 29 May 2025; Received in revised form 21 August 2025; Accepted 29 August 2025
Available online 31 August 2025

systems via fusion-based methods with a focus on AM processes. Several studies have reported successful multi-material manufacturing of pure Cu and Ni using L-DED [9] and L-PBF [10,11] across the whole composition range. Moreover, defect-free samples were reported when processing Ni alloy (IN625) on pure Cu via L-DED, resulting in the presence of two distinct face-centered cubic (FCC) phases [12]. Similarly, a sound interface was established between pure Cu and Ni-2.5Si-1.4B (Delero-22) alloy by L-DED [13].

However, during the printing of various Cu- and Ni-based alloys, extensive cracking was reported. In two similar studies, El Hassanin et al. investigated the processing of 5–20 wt% and 40 wt% Cu-IN718 powder blend parts manufactured via L-PBF [14,15]. They found that at higher Cu contents, heterogeneous microstructures consisting of Cu and Ni-rich regions, with cracks spanning through the melt pool centers and boundaries were present. From this, the authors hypothesized that the cracks occur as a result of increased heat dissipation due to the Cu addition and high shrinkage of copper. Similarly, a heterogeneous microstructure together with cracks lying along the build direction were reported for L-PBF of CuSn10-IN718, where the cracks were attributed to the differences between the thermophysical properties of the two alloys [16]. Zou et al. produced functionally graded parts using CuSn10 and IN718 powder mixtures with 20 vol% composition increments using L-PBF [17]. There, they reported extensive grain boundary cracking in 20, 40, and 60 vol% CuSn10-IN718 compositions and related cracking to the stresses generated due to the differential thermal expansion caused by the addition of copper [17]. In another study, Cu-rich and Ni-rich phase separation, hot and cold cracking were reported during electron beam freeform fabrication (EB-FFF) of Cu8Cr4Nb (GRCop84)-IN625 structures [18]. There, it was proposed that the crack initiation occurred through hot tearing at the Cu-rich zones, whereas crack propagation was due to the local mismatch in yield strength caused by the brittle phases at the interface such as Laves and Cr_2Nb. Another study observed cracking in L-DED of CuSn10-IN718 in addition to secondary phase formation between Cr, Mo, and Nb elements, which showed segregation at the interface [19]. A similar study reported extensive cracking at the grain boundaries along with a heterogeneous microstructure during L-DED of CuSn10-IN718, where the researchers related cracking to insufficient melt pool overlaps and differential thermal expansion and contraction rates of the two materials [20]. Two mechanisms related to liquid state immiscibility were proposed for cracking of Cu4Cr2Nb (GRCop42)-IN625 via metallurgical analyses after arc melting the two alloys [21]. It was stated that solidification cracking occurs for compositions between 30 and 50 wt% Cu4Cr2Nb, whereas cracking due to brittle phases occurs for compositions between 60 and 95 wt%. In another study by the same group, Cu4Cr2Nb-IN625 parts were manufactured in two different depositional sequences [22]. No cracking was observed when IN625 was deposited onto Cu4Cr2Nb. However, cracking did take place when Cu4Cr2Nb was deposited onto IN625 with low power, whereas it was avoided when high power was used. It was shown that different amounts of brittle intermetallics form depending on the attained composition during the liquid phase separation, which was dictated by the heat-input-driven mixing at the interface. As a result, it was proposed that the brittle intermetallics formed in the Cu-deprived liquid led to cold cracking when low heat input is used [22].

As evidenced by the literature review compiled in Table 1, it is apparent that cracking is a common problem when combining Cu alloys and Ni alloys rather than their pure forms. Although the majority of studies presented an explanation for cracking, to the authors' best knowledge, a general framework that combines observations in multiple studies has yet to be established.

One reason for the existence of competing mechanisms describing cracking in Cu- and Ni-based alloy combinations is the fact that they rely on ex situ and post-mortem characterization of microstructure and cracking. Therefore, the hypotheses vary depending on the characterization methods and their interpretation regarding the events that occur during printing. In this regard, in situ and *operando* synchrotron X-ray based experiments during AM have become important tools to understand phenomena that occur during processing [23]. These techniques allow, among others, investigating pore and defect formation [24–28], crack formation and propagation [29–32], phase formation [33,34], thermal history evolution [35–38], and algorithm training and model validation [39–41]. These studies have enabled researchers to better understand underlying mechanisms and competing hypotheses as they yield insight into real-time events.

The current study investigates the cracking behavior of the CuCrZr-IN625 multi-material alloy system during L-PBF. *Operando* X-ray diffraction and imaging experiments were utilized to understand both microstructure and crack formation during processing. Post-processing characterization techniques such as scanning electron microscopy (SEM), energy-dispersive X-ray spectroscopy (EDS) and electron backscatter diffraction (EBSD) coupled with theoretical and thermodynamic calculations were used to complement the in situ experiments. From this analysis, the most crack susceptible range for CuCrZr-IN625 combination was determined theoretically and further validated by printing mixtures of the two alloys. This combined with the *operando* X-ray data helped us formulate a cracking mechanism for this multi-

Table 1
Summary of multi-material manufacturing of Ni-Cu alloy combinations and reported results.

Material Combination	Process	Issues	Proposed Mechanism	Ref.
Cu – Ni	L-DED	-	-	[9]
Cu – Ni	L-PBF	-	-	[10, 11]
Cu – IN625	L-DED	-	-	[12]
Cu – Ni−2.5Si−1.4B	L-DED	-	-	[13]
Cu – IN718	L-PBF	Heterogeneous microstructure and cracking	Rapid heat dissipation and high shrinkage of copper	[14, 15]
CuSn10 – IN718	L-PBF	Heterogeneous microstructure and cracks lying in the build direction	Difference in thermophysical properties of the two alloys	[16]
CuSn10 – IN718	L-PBF	Extensive grain boundary cracking in 20, 40 and 60 vol% CuSn10-IN718 mixtures	Differential thermal expansion caused by the addition of copper	[17]
Cu8Cr4Nb - IN625	EB-FFF	Cu-rich segregation, hot and cold cracking	Solidification cracking due to melting point depression and local mismatch in yield strength	[18]
CuSn10 – IN718	L-DED	Cracking along build direction	Possible secondary phase formation between Cr, Mo, and Nb	[19]
CuSn10 – IN718	L-DED	Heterogeneous microstructure and cracking at the grain boundaries	Insufficient melt pool overlaps and differential thermal expansion and contraction rates	[20]
Cu4Cr2Nb – IN625	General – Arc Melting	Cracking in both lower and upper mixing range of the two alloys	Solidification cracking and brittle intermetallic formation due to liquid immiscibility	[21]
Cu4Cr2Nb – IN625	L-DED	Cracking when Cu4Cr2Nb was deposited onto IN625 with low power	Brittle intermetallic formation in the Cu-deprived liquid due to immiscibility	[22]

material combination during AM. These findings provide important insight into multi-material 3D printing, especially in the case of processability Cu-Ni alloy combinations.

2. Experimental details

2.1. Powder feedstock

Gas-atomized CuCrZr, IN625, and pure Ni (pNi) powders (99.5 wt% pure) in 15–63 μm size range were used in the study. IN625 and pNi powders supplied by GoodFellow Cambridge Ltd. (Huntingdon, England) were used for *operando* X-ray diffraction experiments and ex situ prints, respectively. For all other experiments, CuCrZr and IN625 powders supplied by m4p Material Solutions GmbH (Magdeburg, Germany) were used. Table 2 shows the chemical compositions of the powders.

2.2. L-PBF equipment and parameter space

Operando X-ray diffraction and imaging experiments were conducted using the miniature L-PBF equipment (MiniSLM) developed at Paul Scherrer Institute (PSI), Switzerland. It can be employed at synchrotrons for in situ and *operando* studies of L-PBF. It has been used for both X-ray diffraction and imaging experiments previously [30,35]. The necessary technical details regarding the MiniSLM can be found in [42].

To understand the effect of composition on cracking behavior, powders of CuCrZr and IN625 were mechanically mixed in ratios ranging between 10 and 90 wt% CuCrZr – balance IN625 in 10 wt% increments (Table 3). Since the MiniSLM requires a small amount of powder for each trial (30–50 g), mixing was done by putting the two powders in a container and shaking manually. This simple approach was sufficient to obtain a uniform distribution of powder, as validated by the SEM/EDS investigation shown in Supplementary Figure S1 for the 50 wt % CuCrZr-IN625 mixture. For each powder mixture, two parameter sets with low (L) and high (H) power, respectively, were used to study the effect of energy input on cracking. As CuCrZr and IN625 have vastly different thermophysical properties, it is difficult to obtain the same thermal history for different mixture ratios. Material properties such as absorptivity [43,44] and thermal conductivity [45] are a nonlinear function of the mixture. Therefore, first, the low-energy parameters were developed for each combination to obtain dense specimens. As it is known that solidification cracking is favored by higher energy inputs [46,47], the high-energy parameter sets were then defined by positive power offsets between 40 and 50 W, depending on the CuCrZr content. In this work, the laser power was used as the variable parameter, since the effective absorptivity of CuCrZr powder increases with increasing laser power [48]. Therefore, laser power has a greater influence on the heat input when processing reflective materials such as CuCrZr.

To isolate the effect of alloying elements, the same experiments were repeated using mixtures of CuCrZr-pNi powders instead of IN625. In addition, 20 layers of CuCrZr were printed on top of a pNi part, later to be compared to the CuCrZr-IN625 part in the *operando* XRD experiment. The parameters used for the ex situ prints are shown in Table 3.

Table 3
Process parameters used for the prints. Mixture naming indicates the weight percentage of CuCrZr and IN625 or pNi (e.g., 10Cu90In indicates 10 wt% CuCrZr - 90 wt% IN625). L and H indicate low and high energy parameter sets for the mixtures, respectively.

Alloy / Mixture	Laser Power (W) L / H	Scan Speed (mm/s)	Hatch Distance (μm)	Layer Thickness (μm)
CuCrZr	350	600	70	30
IN625	140	250	50	30
Pure Ni	160	250	50	30
10Cu90In/pNi	140 / 180	250	50	30
20Cu80In/pNi	150 / 190	250	50	30
30Cu70In/pNi	160 / 200	250	50	30
40Cu60In/pNi	180 / 225	250	50	30
50Cu50In/pNi	200 / 250	250	50	30
60Cu40In/pNi	225 / 275	250	50	30
70Cu30In/pNi	250 / 300	250	50	30
80Cu20In/pNi	275 / 325	250	50	30
90Cu10In/pNi	300 / 350	250	50	30

2.3. Operando X-ray characterization

2.3.1. Diffraction experiments

X-ray diffraction experiments were conducted at P21.2 beamline at PETRA III, Deutsches Elektronen-Synchrotron (DESY) in Hamburg, Germany. The X-ray energy and beam size were set to 52 keV and 50×30 μm^2 ($x \times z$), respectively. The X-ray beam was positioned at the last printed layer just below the powder layer where the diffraction patterns of both the powder and the part were visible. The diffraction patterns were collected with a frequency of 1 kHz and an exposure time of 1 ms using an Eiger4M (DECTRIS, Switzerland) detector. The experiments were conducted in transmission mode, where the MiniSLM was tilted at 5° around the *x*-axis (see Fig. 1a).

Prior to the *operando* experiment, a rectangular IN625 part with a cross-section ($x \times y$) of 4×1 mm^2 and height (z) of 2 mm was printed on a pNi baseplate. Then, powder was changed to CuCrZr and additional layers were printed. A bidirectional hatching strategy along the short edge (y) was used for printing CuCrZr. The parameters listed for IN625 and CuCrZr in Table 3 were used for both materials.

The collected 2D diffraction patterns were azimuthally integrated using the pyFAI Python library [49] to obtain 1D XRD profiles. LaB_6 powder was used as standard to calibrate detector position and tilts. Background subtraction was applied to 1D XRD profiles by subtracting a 9th degree polynomial that was fit to the smallest value of every $\Delta 2\theta = 0.8°$.

Table 2
Chemical composition of the powders used in the study, as supplied by the manufacturers.

Material	Supplier	Elemental Composition (wt%)						
Pure Ni	GoodFellow	Co	Cu	Fe	C	O	Ni	
		< 0.50	< 0.09	< 0.15	< 0.06	< 0.16	Bal.	
IN625	GoodFellow	Cr	Mo	Fe	Nb	C	O	Ni
		20.80	8.90	4.00	3.70	0.02	0.02	Bal.
	m4p	Cr	Mo	Fe	Nb	C	O	Ni
		21.30	8.30	3.80	3.30	0.01	0.02	Bal.
CuCrZr	m4p	Cr	Zr	O	Cu			
		0.90	0.07	0.04	Bal.			

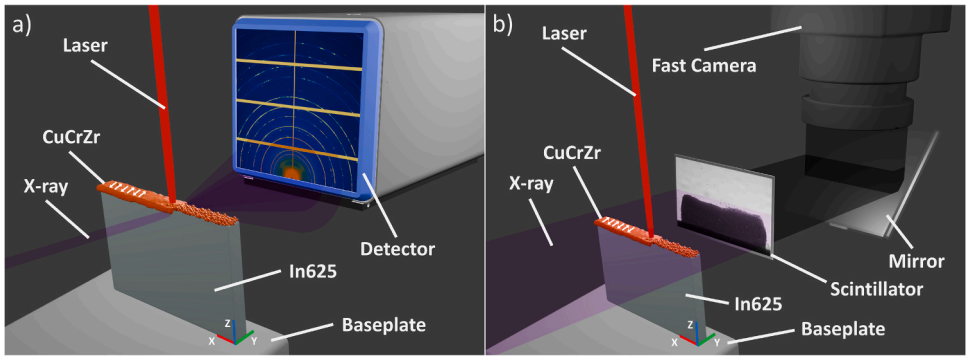

Fig. 1. Schematic representations of the *operando* X-ray a) diffraction and b) imaging setups. White arrows show scanning vectors.

2.3.2. *Imaging experiments*

X-ray imaging (radiography) experiments were conducted at ID19 beamline at the European Synchrotron Radiation Facility (ESRF) in Grenoble, France. A polychromatic X-ray beam with a peak energy of 45 keV was used. A CMOS-based camera (Photron, type: SAZ, Japan) lens-coupled (10x magnification, 0.28 numerical aperture, Mitutoyo, Japan) to a 250 μm thick LuAG:Ce crystal scintillator was used for image acquisition. Sample and optical setup allowed the use of a 40000 images/s acquisition rate to collect X-ray radiographs with a resolution of 2.2 μm/pixel during the manufacturing process. Contrast was boosted by propagation-based phase contrast thanks to the partially coherent illumination at beamline ID19.

First, a rectangular IN625 part with dimensions of $9 \times 1 \times 3$ mm^3 ($x \times y \times z$) was built on a pure nickel baseplate. Then, both sides of the wall were ground down to 0.3 mm thickness with P1200 sandpaper. Finally, CuCrZr powder was deposited onto the IN625 part using the recoater of the MiniSLM to control the layer height. To have sufficient X-ray transmission and be able to acquire images, the powder surrounding the part was removed. CuCrZr powder was melted using the same parameters as in the diffraction experiments. The imaging setup is schematically shown in Fig. 1b. FIJI (ImageJ) [50] software was used to process images with flat field correction, sharpening filter and brightness/contrast adjustments.

2.4. *Thermodynamics calculations*

To understand phase formation and solidification behavior of the combined alloys, ThermoCalc® [51] with TCHEA5 database was used to calculate the IN625-Cu material-material isopleth, determine one-axis phase plots, and perform Scheil-Gulliver calculations. For simplicity, only Cu, Ni, Cr, Mo, Fe, and Nb elements were considered where CuCrZr was assumed to be pure Cu. In addition, only FCC and liquid phases were considered as no other phase was experimentally detected in any of the samples.

First, IN625-Cu material-material isopleth was calculated to understand the metastable equilibrium behavior with respect to the temperature and amount of mixing between the two alloys. Then, to investigate cracking susceptibility, Scheil-Gulliver calculations were performed considering the same mixing ratios as in the ex situ prints presented in Table 3.

The Kou model [52] was used to assess solidification cracking susceptibility of different mixing ratios. During the solidification of alloys in processes such as casting, welding and additive manufacturing, directional solidification of cellular or columnar dendritic grains is often observed. Since alloys generally solidify over a temperature range, there exists a mushy zone involving liquid and solid phases during solidification. Due to the density difference between solid and liquid as well as the stresses generated due to inhomogeneous thermal contraction of the solid during solidification, the mushy zone, which has little strength, separates into cracks at the grain boundaries. Based on these, the Kou model predicts the cracking susceptibility of an alloy using:

$$CSI = \left| \frac{dT}{d(f_s)^{1/2}} \right|_{\max} \quad (1)$$

where *CSI* is the cracking susceptibility index, T is the temperature, and f_s is the solid fraction. The model states that the maximum slope of the T versus $f_s^{1/2}$ graph (close to complete solidification) is a measure for cracking susceptibility.

In the original article, the *CSI* is calculated by taking the average slope in an arbitrarily selected f_s range close to complete solidification [52]. However, subsequent articles have adapted to calculate *CSI* using the maximum slope before complete solidification [53–55], where extensive bridging between the dendrites was assumed to occur at $f_s = 0.99$. The latter approach was adopted in this study as it offers more objective calculations.

2.5. *Post-mortem characterization*

All samples were cut from the baseplate using a wire saw and hot mounted in resin on their side (*x-z* plane in Fig. 1). They were ground using sandpapers with grits down to P4000 and finally down to 1 μm finish using diamond suspension.

Optical microscopy (Keyence, VHX-5000, Japan) was used to investigate cracks after further polishing using 0.25 μm oxide polishing suspension. FIJI (ImageJ) [50] software was used to measure crack density of the parts using user-defined grayscale thresholding and *analyze particles* routine where segmented objects with a circularity above 0.35 were ignored. To obtain better statistics, the measurements were repeated three times on repolished sections. Crack number density was adopted as the closest measure of the potential of forming cracks that can be compared to the calculated *CSI* values.

To investigate microstructure and composition using SEM, the sample from the XRD experiment was polished using an Ar-ion polisher (Hitachi, IM4000, Japan) for 5 min at an accelerating voltage of 6 kV and a tilt angle of 5°. An SEM (Zeiss, ULTRA 55, Germany) equipped with both in-lens and external (Everhart-Thornley, ETD) detectors, an EBSD detector (EDAX, Hikari, Japan), and an EDS (Oxford, ULTIM EXTREME, United Kingdom) detector was used. For SEM/EDS analysis, accelerating voltages of 10 and 20 kV were used. Due to the fine scale of the observed microstructures, EDS maps of the polished cross-sections were collected at 10 kV to reduce the electron beam interaction volume and minimize signal interferences. On the other hand, 20 kV was used for the EDS maps of the powder mixtures given in Supplementary Figure S1 to obtain better statistics. EBSD analyses were conducted at 20 kV accelerating voltage and 0.1–0.2 μm step size. 90 % of the collected data points had a confidence index (CI) greater than 0.1. EBSD data were cleaned by neighboring CI correlation using TSL OIM Analysis 8.1.0, where no more than 10 % of the points were changed following ASTM E2627 [56].

3. Results

3.1. Calculated phase evolution

Fig. 2 shows the metastable isopleth of Cu-IN625 material-material system calculated using ThermoCalc. The isopleth shows a single liquid phase above 1980 °C. However, at lower temperatures, for compositions ranging between 12 and 98 wt% Cu, the liquid separates into two parts consisting of Cu rich (L_{Cu}) and Ni rich (L_{Ni}) regions. This behavior stems from the large positive enthalpy of mixing between Cu and the alloying elements (Cr, Fe and Mo) in IN625 [57]. Figs. 3a and 3b show, respectively, the calculated volume percentage of phases and corresponding composition profiles with respect to temperature under metastable equilibrium for a 50 wt% Cu-IN625 mixture. These demonstrate that upon further cooling, L_{Cu} is depleted of the mentioned alloying elements. These then migrate into L_{Ni}, with approximately 20 wt% Ni remaining in L_{Cu}.

A monotectic reaction is observed in Fig. 2 at 1300 °C and 18 wt% Cu, where the liquid (Ni-rich) transforms into γ-Ni (FCC) + L_{Cu}. Between 12 and 95 wt% Cu in Fig. 2, L_{Cu}, L_{Ni} and γ-Ni coexist between the monotectic reaction boundary and the phase boundary below, which extends down to 1120 °C at 92 wt% Cu. In the same composition range, γ-Ni forms from L_{Ni} below this boundary (L_{Cu} + γ-Ni region), and the remaining L_{Cu} subsequently transforms to α-Cu upon further cooling. Between 88 and 96 wt% Cu, L_{Ni}, L_{Cu}, γ-Ni and α-Cu coexist at 1100 °C, below which L_{Cu} forms α-Cu, and L_{Ni} that is enriched in Cr and Mo forms the last γ-Ni solid. For compositions above 98 wt% Cu, a single α-Cu (FCC) phase forms from L_{Cu}. Similarly, for compositions lower than 12 wt% Cu, L_{Ni} transforms into a single solid (γ-Ni). For the same composition range, a Cu-rich FCC phase is expected to form in solid state. However, a two-phase microstructure with distinct compositions was not readily observable in the EDS maps of the 10 wt% CuCrZr-IN625 mixtures as shown in Supplementary Figure S2. This could be attributed to the high cooling rates experienced during L-PBF.

It is important to note that when the BCC phase is included in the calculations, the Cr- and Mo-enriched L_{Ni} would start solidifying into a BCC phase at a much higher temperature than the formation of α-Cu (see Supplementary Figure S3). However, as no BCC phase was detected in any of the characterized samples during X-ray diffraction measurements, it was decided to not include it in the main calculations. Therefore, the assumption of considering only liquid and FCC phases is kept for the main discussion of this study. In addition, the discussion focuses on the composition range where the BCC is not expected to form (Supplementary Figure S3).

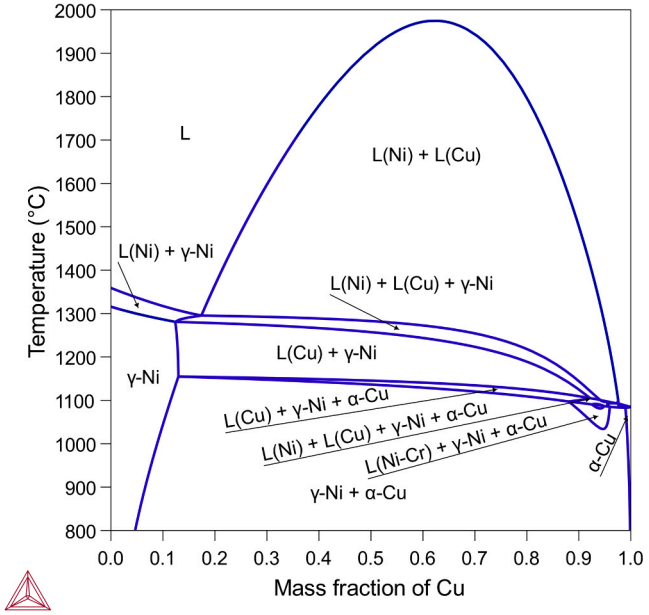

Fig. 2. Metastable isopleth of IN625 – Cu pseudo binary system.

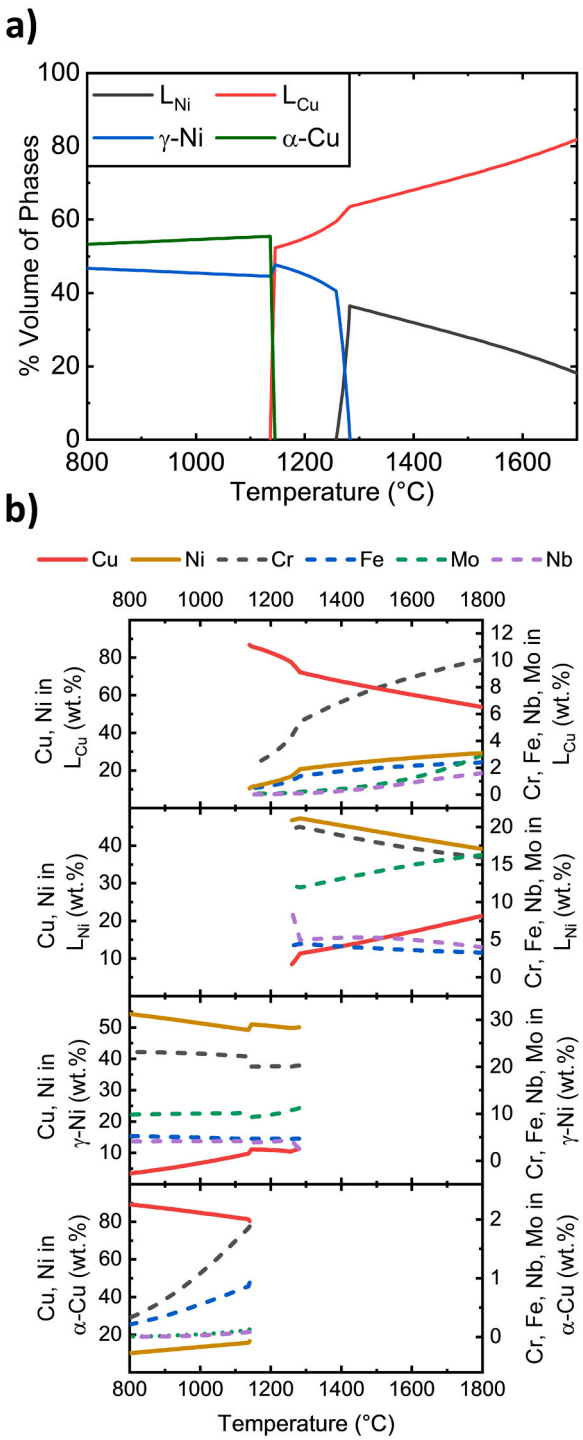

Fig. 3. Calculated a) volume percentage of phases and b) corresponding composition profiles with respect to temperature under metastable equilibrium for 50 wt% Cu-IN625 mixture. Left scale in b) denotes the amount of Ni and Cu whereas the right scale denotes Cr, Fe, Nb, and Mo in weight percent.

3.2. Operando X-ray diffraction, phase formation and cracks at the interface

Fig. 4a shows the cross-section of the sample produced during

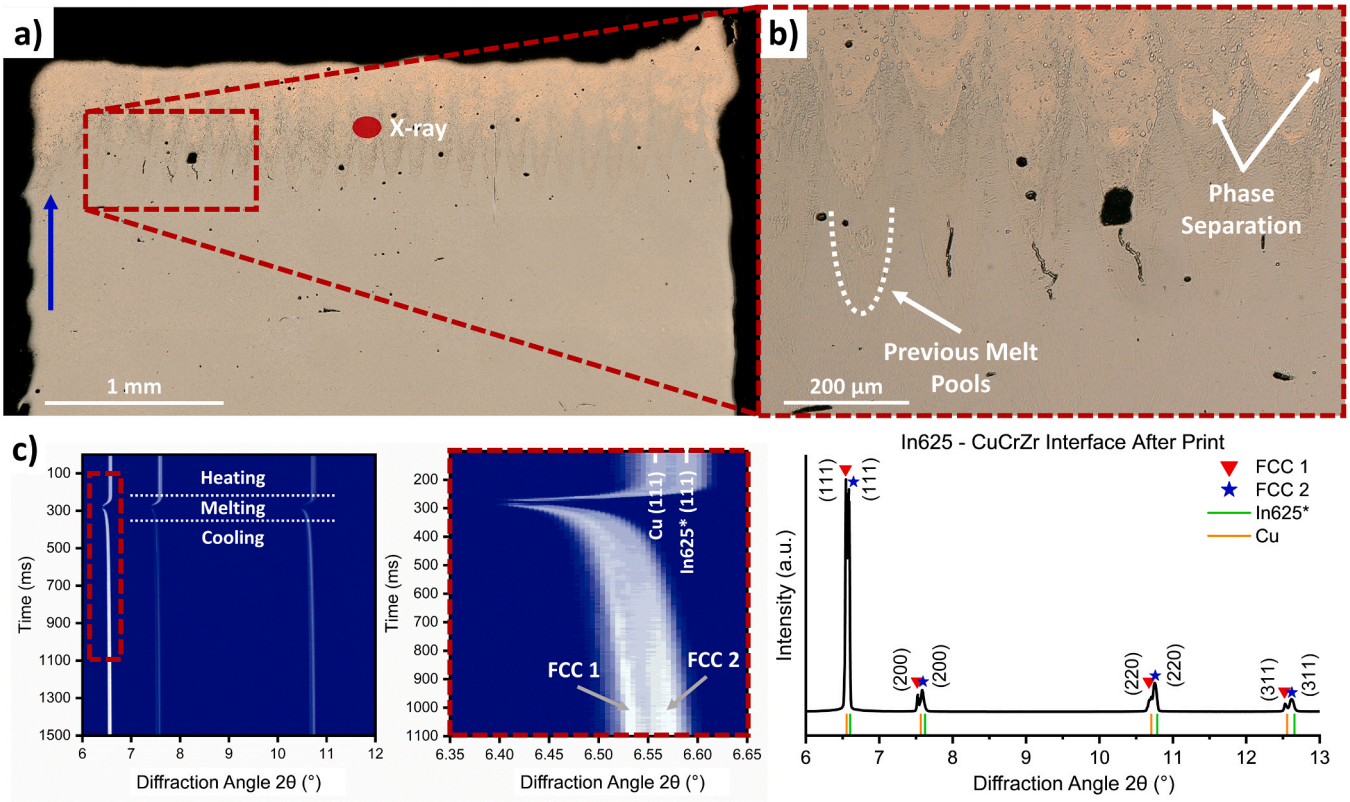

Fig. 4. a) Low and b) high magnification optical micrographs of the CuCrZr-IN625 sample produced during *operando* XRD experiments showing cracks, previous melt pools, phase separation, and approximate X-ray beam position. Blue arrow indicates the build direction for both micrographs. c) XRD pattern evolution during L-PBF process and at the end of cooling. *Angular positions of the reflections were calculated based on the standard average composition of IN625 using Vegard law coefficients supplied in [58].

operando XRD experiments as well as the approximate X-ray beam position. In a close-up to the interface, Fig. 4b shows spherical gray droplets in and around the copper-colored melt pools, where the color contrast reveals the phase separation between the Cu-rich and Ni-rich regions. In this image, there are three cracks observed at the tip of three melt pools, where the Cu concentration appears lower based on the color contrast. This has been further evidenced by the EDS maps taken from the region right above the cracks as shown in Supplementary Figure S4.

Waterfall plots in Fig. 4c depict the phase evolution during laser melting and solidification at the position of the X-ray spot shown in Fig. 4a, while the corresponding layer was being built. The process starts with two side-by-side peaks that belong to CuCrZr powder and the IN625 part. Upon heating by the laser, position of the peaks shifts to lower angles due to lattice expansion, then disappears for about 20 ms due to melting. During subsequent cooling, two FCC phases appear and rise in intensity due to solid formation. At the end of cooling, two FCC phases remain with similar peak positions as the initial Cu and IN625 powder lines.

The crack at the center in Fig. 4b was observed under SEM as shown in Fig. 5a. The crack appears to have initiated from the center of the melt pool. Following the EBSD inverse pole figure (IPF) + image quality (IQ) map in Fig. 5b, it can be seen that there are regions of small and equiaxed grains with random orientation distributed within large grains. Lower magnification EBSD IPF + IQ map of this region and the corresponding orientation distributions are given in Supplementary Figures S5a and 5b, respectively. As seen in the figure, large columnar grains show a strong texture along the build direction, confirming literature outcomes for nickel-based alloys [59]. Accordingly, Supplementary Figure S6a and b show two SEM images taken from the surface of the sample from the *operando* X-ray imaging experiment, where the substructure of the columnar grains consists of mainly cellular grains with some dendritic side branches occasionally visible.

As highlighted by the EDS elemental maps shown in Fig. 5c, equiaxed grains and large textured grains are respectively observed in areas with Cu segregation and the alloying elements of IN625. Crack initiation point appears to be at the center of the melt pool, in the middle of a Cu-enriched region. Droplets of Cu-depleted regions within the Cu-rich areas are also visible in Fig. 5c. EDS elemental maps in Supplementary Figure S4c further show the elemental segregation in and around the melt pools as observed in Fig. 4b by the color contrast, which appear as dark and bright in the SEM image for Cu-rich and Ni-rich phases respectively. Supplementary Figure S7 shows EDS elemental maps acquired at the edge of one melt pool together with the positions of EDS point analyses from the dark- and bright-contrast regions, results of which are shown in Supplementary Table S1. The alloying elements are mostly contained within the Ni-rich (dark contrast) phase together with 18–26 wt% Cu, whereas the Cu-rich (bright contrast) phase primarily consists of Cu and Ni (14–21 wt%), with 2–4 wt% Cr.

It must be noted that the limited contrast in some EDS maps (e.g., Fe, Ni, and Cr) in Fig. 5c and Supplementary Figure S7 is due to the use of 10 kV accelerating voltage and L_α X-ray emission lines, which provide lower peak separation and signal clarity, especially for elements like Fe with low concentration. This acceleration voltage was selected to minimize the electron beam interaction volume and effectively distinguish micron-sized droplets visible in Supplementary Figure S7. Additional signal overlap arises from the fine Ni-rich droplets within Cu-rich regions and the partial solubility of Ni and Cr in α-Cu. While K_α lines offer better contrast, they require longer dwell times unsuitable for mapping at this accelerating voltage. Quantitative point analyses using full spectrum fitting in Supplementary Table S1 mitigate these limitations, thus, providing better precision.

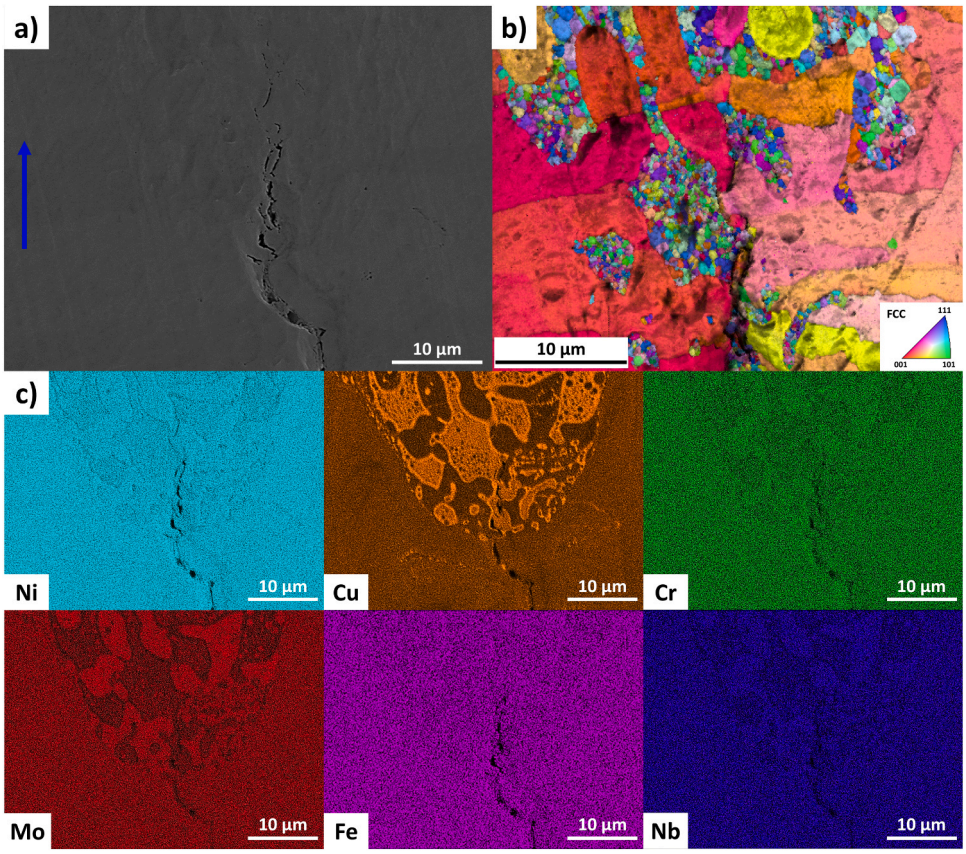

Fig. 5. a) SEM image (ETD-detector) showing the crack in a melt pool, b) corresponding EBSD IPF+IQ map and c) EDS elemental maps from the same region. Blue arrow indicates the build direction. EDS maps were acquired at 10 kV and show L_α signals.

3.3. *Operando X-ray imaging of crack formation*

Fig. 6 shows the radiographic time series during the printing of two tracks (laser scanning direction is in and out of the screen/page). The full video is available in Supplementary Video 1. Initially, for Track 3 and Track 5, the bump from previous tracks and CuCrZr powder particles are visible on the IN625 sample at t_0. The keyholes created by the laser are visible as shown by the yellow arrows. After the laser passes, the boundaries of the melt pools (molten region) are visible as shown by the red arrows. The liquid area shrinks towards the center of the melt pool as solidification proceeds. Just before complete solidification, the center of the melt pool separates into a crack (visible as a brighter contrast) for both Track 3 and 5. The same behavior can be observed in multiple tracks in Supplementary Video 1, where adjacent tracks heal the previously formed crack in some examples.

3.4. *Cracking in powder blends*

Fig. 7 shows the cracking behavior for 10–60 wt% CuCrZr-IN625 powder blends processed with H parameter sets, where cracks elongated in the build direction are visible from 20 to 40 wt% CuCrZr. No cracks were observed outside this range. A similar behavior is observed for the L energy parameter sets. Interestingly, all CuCrZr-pNi samples were crack-free. Moreover, there is no visible phase separation for CuCrZr-pNi powder blends. The results of the full parameter space, including L and H parameter sets and CuCrZr-pNi mixtures, are shown in Supplementary Figure S8.

Quantitative measurements of crack density, i.e., number of cracks per unit area, for CuCrZr-IN625 powder blends are shown in Fig. 8. The measurements support previous qualitative observations for which cracks are observed solely in the range of 20–40 wt% CuCrZr. However, cracking peaks at different mixture ratios depending on the parameter set: 30 wt% and 40 wt% CuCrZr for H and L parameter sets, respectively.

4. Discussion

As presented in the introduction, to our best knowledge, cracking has not been reported in the literature when pure Cu and Ni are processed together. Similarly, considering Cu-Ni binary phase diagram [60], printing CuCrZr onto pNi was expected to result in formation of a single liquid and a single FCC phase with a composition gradient over the interface, considering that there is negligible alloying in the system. This is indicated by the lack of clear phase separation (i.e., into droplets) in Supplementary Figure S9. As such, no cracks were observed in this sample.

On the other hand, there have been numerous studies in the literature that reported cracking in different Cu-Ni alloy combinations, with each study proposing specific mechanisms of crack formation. Although some of these are indeed specific to the systems studied, such as formation of intermetallics, the others lack a comprehensive understanding that can be translated to other systems. Here, based on the observations in the literature and this study, it is aimed to draw a comprehensive mechanism that can explain cracking in different Cu-Ni alloy combinations. In this regard, alloying elements play a primary role, where liquid phase separation induced by the large mixing enthalpy of Cu with Cr, Fe and Mo in IN625, separates the material into two species with vastly different melting points, leading to solidification cracking as will be explained in the following sections.

4.1. *Phase formation and microstructure evolution during printing*

Due to the alloying elements in the CuCrZr-IN625 system, phase

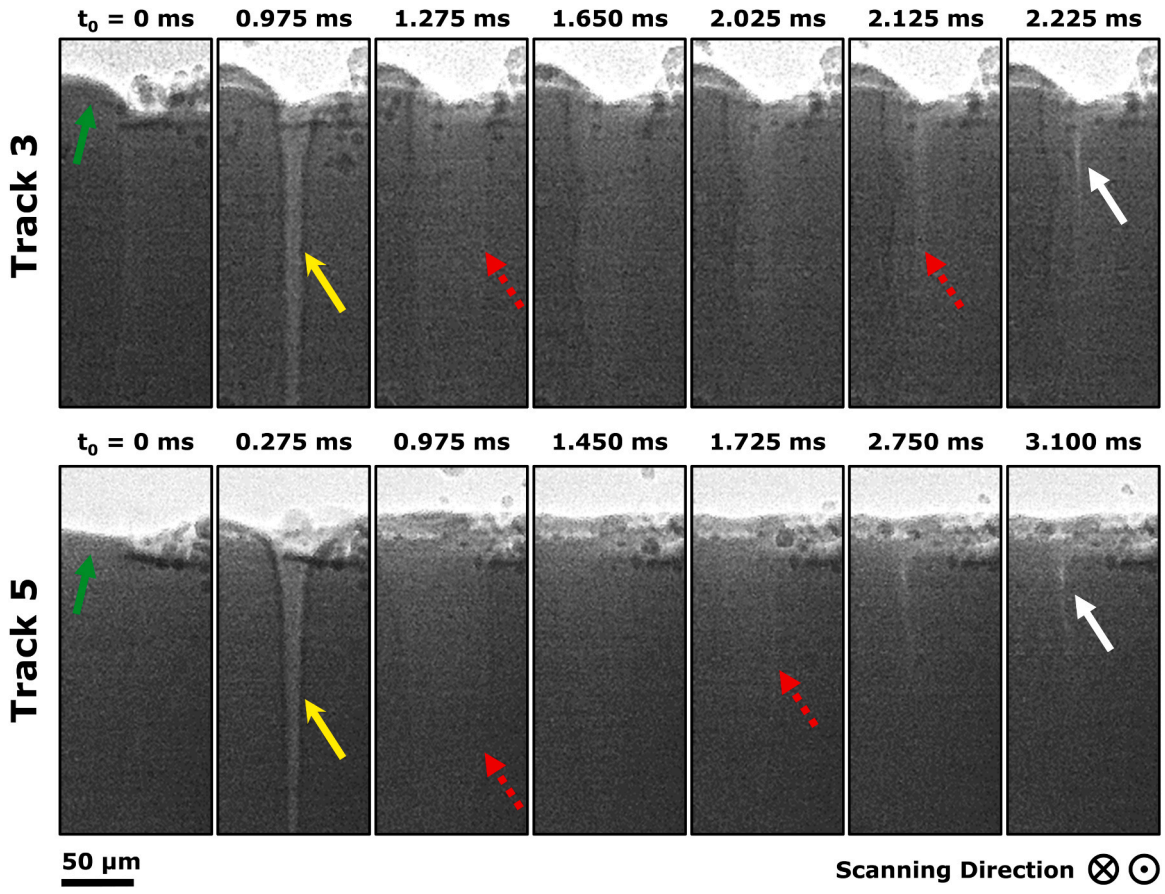

Fig. 6. X-ray radiographs showing melting, solidification, and crack formation during printing. Green arrows show the bump from previous tracks, yellow arrows show the keyhole induced by the laser during scanning, dashed red arrows show the melt pool boundary after the laser pass, and white arrows show the cracks. Scale bar is common to all images.

hierarchy is driven by the mixture ratio. As introduced previously, assuming that the kinetics are sufficiently fast in the liquid state to initially form a homogeneous liquid at high temperature, any composition between 12 and 95 wt% CuCrZr ends up with different fractions of L_{Cu} and L_{Ni}. When CuCrZr powder is deposited and melted by the laser, the underlying IN625 part mixes with CuCrZr in the melt pool, with higher amounts of CuCrZr over successive layers, creating a composition gradient. For most parts of the discussion, it can be reasonably assumed that this gradient falls within the 12–95 wt% CuCrZr range.

According to Fig. 3b, L_{Ni} should contain 10 wt% Cu and 20 wt% Cr before solidification begins and γ-Ni should have a maximum solubility of 12 wt% Cu and 23 wt% Cr. However, as seen in the point EDS analysis in Supplementary Table S1, Ni-rich regions of approximately 20 wt% Cu and 16 wt% Cr were observed. This can be explained by the mass transport dominated liquid phase separation before solidification. When liquid phase separation starts, to minimize its surface energy, L_{Ni} forms as spherical droplets in L_{Cu} with the initial composition shown in Fig. 3b, i.e., approximately 21 wt% Cu and 16 wt% Cr at 1800 °C. At lower temperatures, L_{Ni} droplets form with lower Cu and higher Cr contents as predicted in Fig. 3b. At the same time, the droplets of previously formed L_{Ni} start rejecting Cu and dissolving Cr at the L_{Ni}/L_{Cu} interface. However, due to the high cooling rates, this process cannot reach completion before the start of solidification. As a result, some droplets retain higher amounts of Cu and lower amounts of Cr compared to the others after solidification. A similar behavior was observed in fast cooling of immiscible Cu-Co [61] and Cu-Fe [62] melts. After the phase separation in liquid state, γ-Ni starts nucleating preferentially on the columnar grains of previous layers, or nucleate as dispersed islands in the L_{Cu}, as observed in Fig. 5. Then, the competitive growth of γ-Ni starts towards the center of the melt pool, where the direction of maximum heat extraction coincides with the easy growth direction of the cells or dendrites. Although the substructure within the columnar grains are too small to resolve, Supplementary Video 1 shows the liquid boundary shrinking towards the center of the melt pool clearly. During the growth of γ-Ni in presence of L_{Cu} and L_{Ni} just below the monotectic temperature; Cr, Mo, Fe, and Nb are rejected from L_{Cu}, which were then redistributed among L_{Ni} and γ-Ni. In the further stages where only γ-Ni and L_{Cu} remain (1240–1140 °C), the latter is used to form more γ-Ni as L_{Cu} becomes purer in Cu while still maintaining some Ni (see Fig. 3b). At this stage, L_{Cu} is present as disconnected regions within the melt pool.

As previously mentioned, γ-Ni droplets solidify inside L_{Cu} after liquid phase separation. These Ni-rich droplets within the Cu-rich regions are visible in Fig. 5c and Supplementary Figure S7c. Solidification of α-Cu only becomes possible at lower temperatures (below 1140 °C), where the fine γ-Ni droplets may act as preferential nucleation sites for α-Cu grains, leading to the formation of fine and equiaxed grains seen in Fig. 5b. This hypothesis can be supported by the fact that Ni- and Cu-rich regions have very similar compositions as given in Supplementary Table S1, and they have a similar lattice parameter as apparent from their diffraction peaks in Fig. 4c. Lattice parameter analysis of the diffraction peaks of the two phases yields a lattice misfit as small as 0.65 %. Therefore, considering that both phases have an FCC structure, γ-Ni droplets can be expected to act as preferential nucleation sites for α-Cu. As shown in the EDS maps in Supplementary Figure S7c, there are areas (shown by the arrows) depleted in Cu with some Ni around the droplets and Ni-rich peninsulas. In addition, regions in between the droplets are richer in Cu. Following the equilibrium composition of α-Cu at the beginning of solidification as shown in Fig. 3, it can be expected

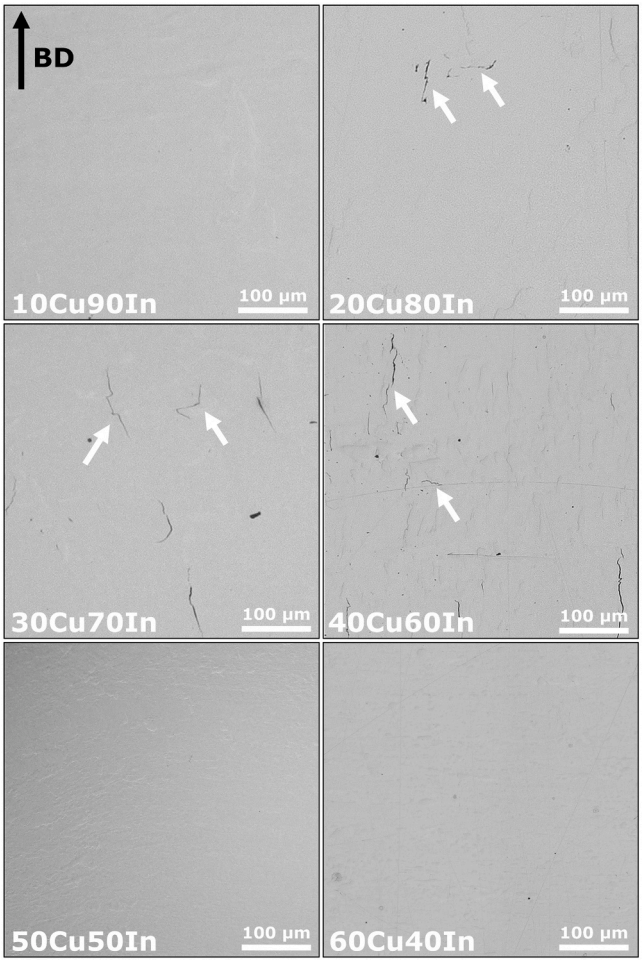

Fig. 7. Optical micrographs from 10 to 60 wt% CuCrZr-IN625 powder blends produced using high energy parameter sets, white arrows indicate cracks. The black arrow shows the build direction for all samples.

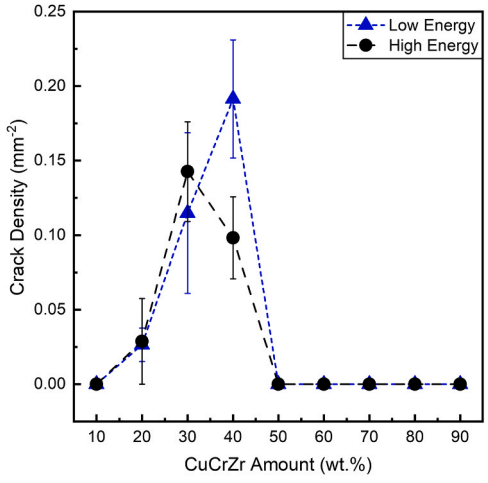

Fig. 8. Crack density of all powder blends processed with low and high energy parameter sets. Error bars represent variation between three observed sections.

that the initial α-Cu has around 18 wt% Ni. Due to the high cooling rate, the transformation cannot complete in the narrow temperature range (1140–1130 °C) shown in Fig. 2. According to the Scheil-Gulliver calculation in Supplementary Figure S10a, α-Cu formation begins at 1140 °C and completes at 1070 °C. The solubility of Ni in α-Cu decreases with temperature, and α-Cu solidifies with less and less Ni as solidification extends to lower temperatures as visible in Supplementary Figure S10b. This behavior is visible in regions shown by the arrows in Supplementary Figure S7c, where there are regions with higher Ni content within the Cu-rich regions. Furthermore, since γ-Ni droplets can act as preferential nucleation sites for α-Cu, the initial α-Cu composition can be attained around them. Therefore, the first α-Cu with higher Ni content can form on these droplets. This is visible as the "halo-shaped" regions indicated by the arrows around some γ-Ni droplets in Supplementary Figure S7c, where the Ni content decreases and the Cu content increases moving away from these γ-Ni/α-Cu interfaces. Here, it should be noted that the other alloying elements are not present (in comparable amounts to γ-Ni regions) in these Cu-rich regions. This indicates that the Cu-rich regions formed from the terminal L_{Cu} that contained only Ni and Cu, essentially.

Consistent with the presented phase evolution, *operando* X-ray diffraction results in Fig. 4c show the formation of two distinct FCC phases during solidification. These phases result from the two distinct liquid compositions that formed due to the miscibility gap and retain upon cooling down to room temperature. Here, the two FCC phases appear to form simultaneously from the melt in Fig. 4c. However, this measurement cannot be relied on for assessing the phase transformation sequence since the volume probed through the sample thickness encompasses regions which are at different stages in the fusion/solidification sequence, and the acquisition rate used in the study is not sufficient to differentiate two FCC phases with overlapping peak positions. For reference, studies investigating such phase transformation sequences use 20–40 times higher acquisition rates [35,63].

4.2. Quantifying the cracking susceptibility

Fig. 9a and b show Scheil-Gulliver plots for 10–90 wt% CuCrZr-IN625 mixtures and corresponding *CSI* values calculated, respectively. Overall, a good agreement is found between the theoretical and experimental values, as well as with previous studies on Cu-Ni alloy mixtures [14,15,21]. High *CSI* values were calculated for the composition range where cracks for both L and H parameter sets were observed. Furthermore, an excellent match is observed when looking at the H parameter subset, where the peak cracking susceptibility occurs at 30 wt% CuCrZr (see Fig. 8 and Fig. 9b). These results, as well as some discrepancies observed between the theory and experiments, are discussed in the following section.

Initially, the Kou model was developed for alloy systems with a single liquid forming a primary phase then undergoing eutectic (or peritectic) reaction. Therefore, it is important to discuss its applicability to immiscible multi-material alloy systems. In the original model, the maximum slope of the T versus $f_s^{1/2}$ graph, thus, the highest cracking susceptibility is observed in the last stages of solidification [52]. After the primary solid formation takes place, the remaining liquid fraction is rather small and insufficient to back-fill the forming cracks. However, in the case of CuCrZr-IN625, the maximum slope occurs much earlier (see black dashed lines in Fig. 9a), as γ-Ni almost completely solidifies before α-Cu even begins to solidify. Therefore, there is plenty of L_{Cu} to back-fill the cracks. Moreover, there are two solidification reactions with a primary phase in the same solidification process, for the solidification of γ-Ni and α-Cu, respectively. Yet, taking the maximum slope before complete solidification (assumed $f_s^{1/2} = 0.99$) still yields reliable results as presented above. This is because *CSI* is in essence a measure of the thermal and phase transformation straining that is applied on the primary phase before the temperature drops sufficiently for solidification to complete. Therefore, the calculated slope coincides with the temperature range in Fig. 2 where γ-Ni formation is almost complete but L_{Cu} has not started solidifying (1240–1140 °C). In addition, although there is a high amount of L_{Cu} present in the cracking range, due to the extended channel length between the cells or dendrites, which increases as *CSI* increases [52], the forming cracks cannot be back-filled. The total length

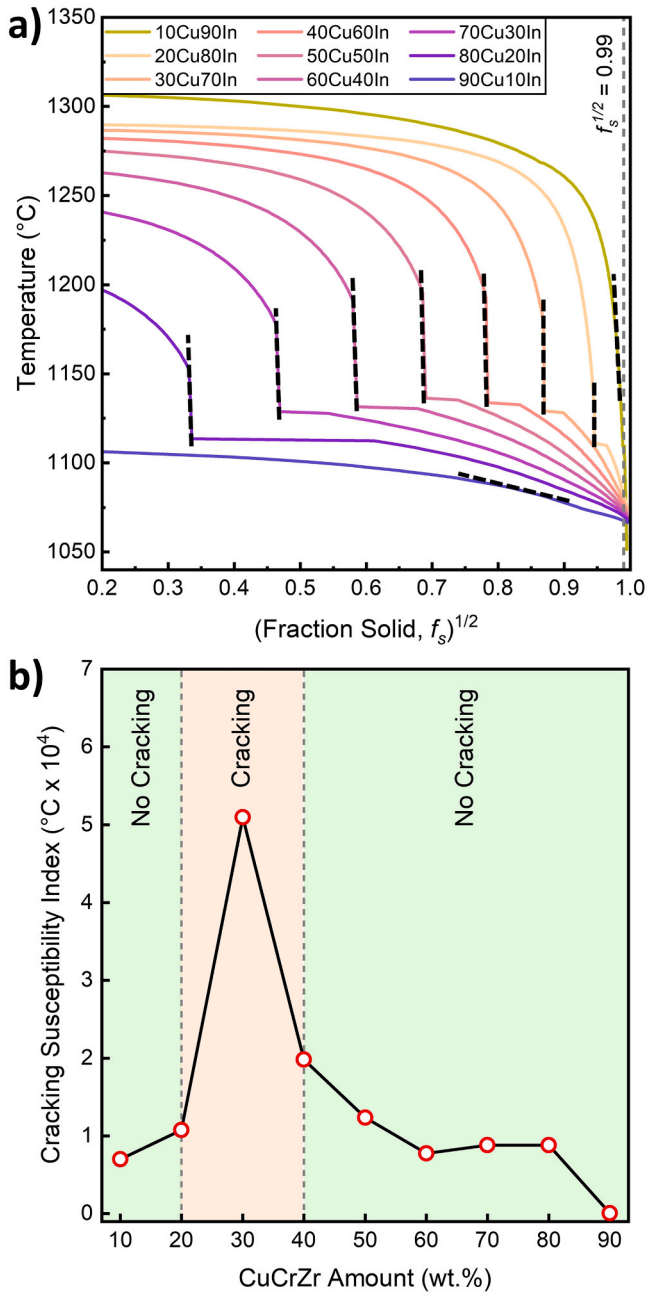

Fig. 9. a) Scheil-Gulliver calculation results and b) corresponding cracking susceptibility index (*CSI*) calculated for CuCrZr-IN625 powder blends. Dashed lines in a) show the maximum slope used to determine *CSI*. The green and light orange colors respectively indicate the range of compositions that cracking was not observed and observed experimentally.

of cracks shown in Fig. 5 can be observed in Supplementary Figure S5. The cracks span over a length of 150 μm, pointing out the long channel length that had to be filled before cracking occurred.

Note that there are no cracks observed for 50 wt% CuCrZr whereas 20 wt% CuCrZr mixture exhibits cracking, despite the fact that the former has higher *CSI*. For the phase formation in mixtures with a higher percentage of CuCrZr than IN625, it is irrelevant to consider the primary epitaxial growth of a γ-Ni phase. Since there is at least equal or greater amount of L_{Cu} as the main matrix, γ-Ni droplets are separated into islands as can be seen in Supplementary Figure S11. Therefore, one of the main assumptions of the Kou model, cellular or columnar dendritic growth of the primary solid, does not apply in this case [52]. As a result, there are no thermal or phase transformation stresses relevant to γ-Ni as a connected body that would crack at the L_{Cu} regions. Optical micrographs of CuCrZr-IN625 mixtures in Supplementary Figure S11 corroborates this statement, where the isolated Ni-rich droplets are visible from the color contrast for mixtures having 50 wt%CuCrZr or more, regardless of the heat input.

As presented in Fig. 8, peak cracking density occurs for different amounts of CuCrZr in the ex situ prints for low and high energy, respectively at 40 and 30 wt% CuCrZr. This can be explained by the different cooling rates and experienced undercooling due to the different processing conditions. As recently shown by Dasgupta and Kou [64], the peak cracking susceptibility shifts to higher Cu contents in Al when the cooling rate is higher. This is because of the greater undercooling experienced at higher cooling rates as a result of kinetic solute partitioning (solute trapping) during growth, and dendrite tip curvature undercooling [64]. Therefore, the position of the largest freezing range as well as the maximum slope (highest *CSI*) shifts in composition. It was also shown that for the same alloy composition, a lower energy input results in less overall heating and hence, faster cooling rates during solidification [65]. Therefore, the behavior in Fig. 8 stems from the fact that the highest crack susceptibility shifts from 30 to 40 wt% CuCrZr when the energy input is lower, which results in higher cooling rates [65] and greater extent of undercooling.

Consistently with the calculated and observed cracking range, three cracks in Fig. 4b took place at the centerline of the melt pools, where the EDS map sum spectrum shows 41.6 wt% Cu. The previous melt pools are visible by the color contrast as indicated by the dashed line in Fig. 4b where cracking had not occurred as the composition was not sufficiently rich in Cu to fall into the cracking window. Hence, cracking occurred in the next layers when more Cu was added. Cracking initiates at the Cu-rich islands at the center-top portion of the melt pool where the columnar grains touch last, and propagates down, as also visible in Supplementary Video 1 and Track 5 in Fig. 6.

Therefore, avoiding the 20–40 wt% CuCrZr composition range is important to mitigate cracks in CuCrZr-IN625 parts. Due to the low laser absorptivity and high thermal diffusivity of copper, CuCrZr requires much higher heat input compared to IN625 to obtain dense parts. As a result, horizontal interfaces where CuCrZr is deposited on IN625 are expected to have deeper melt pools and extensive mixing over the interface. In such cases, if the composition in the melt pool becomes sufficiently diluted in CuCrZr, cracking may occur. Furthermore, deeper melt pools cause columnar grains to grow at higher misorientation angles, which further increases the cracking susceptibility [66]. Yet, if a Cu-rich composition is ensured at the interface when depositing the Cu alloy on top of the Ni alloy, crack-free interfaces can be produced even in the case of pronounced mixing [67]. On the other hand, although less mixing is expected when IN625 is deposited on CuCrZr, the amount of copper dissolution required to induce cracking is significantly lower as the cracking susceptibility window already lies within the Ni-rich compositions. Moreover, thermal and residual stress profiles can be significantly altered when the deposition sequence is changed, as the thermophysical properties of Ni and Cu alloys are significantly different. Hence, in both configurations, process conditions must be adjusted so that the cracking susceptibility window is avoided as well as inhomogeneous thermal gradients, which give rise to pronounced thermal and residual stresses across the melt pool.

In summary, depending on the process conditions, melt pool characteristics and the amount of mixing, both cracks [16,68] and sound interfaces [12,22,69,70] can be observed regardless of the deposition order. A similar cracking behavior is apparent for both configurations in other multi-material systems known to suffer from solidification cracking [71,72]. Following these, certain process modifications have been proven successful for printing crack-susceptible multi-material systems. For instance, using laser beam shaping can create shallower and wider melt pools, which induces less mixing and relatively uniform thermal gradients at the interface of CuCrZr-316L multi-material, yielding an interface with less cracks [73]. Similarly, graded parameter

variations at the interface, laser wobbling and discretized transition zones have been shown to help mitigate cracking in a copper-steel multi-material [74]. Furthermore, utilizing blue lasers has proven effective in obtaining sound Cu-IN718 interfaces [75]. Since copper has much higher absorption rate under blue laser irradiation, extensive heating in the substrate can be avoided, and shallow melt pools with limited mixing can be obtained [75].

4.3. A generalized cracking mechanism in Cu-Ni alloy combinations

The cracking mechanism for the CuCrZr-IN625 combination can be summarized as depicted in Fig. 10. In Step 1, upon laser melting, CuCrZr and IN625 powders mix to form a single liquid phase, although there might be a composition gradient within this phase. In Step 2, phase separation takes place in the liquid state where L_{Ni} assumes spherical shape in L_{Cu} while depleting it in Cr, Mo, Fe, and Nb. Then, competitive growth of γ-Ni with a cellular or columnar dendritic morphology starts towards the center of the melt pool where L_{Ni} droplets also solidify within L_{Cu} (Step 3). In the later stages of solidification (Step 4), L_{Cu} exists as films between the γ-Ni grains. L_{Cu} solidifies last and much later than the complete solidification of γ-Ni. Therefore, tensile thermal contraction stresses keep accumulating on γ-Ni during cooling. Then, solidifying α-Cu depletes the remaining liquid in Ni, which further depresses its solidus temperature. Therefore, the mushy zone composed of γ-Ni/L_{Cu} extends over a wide temperature range where thermal and phase transformation tensile stresses on γ-Ni grains separate the L_{Cu} regions into cracks (Step 5). Finally, the crack further grows in between the cells or dendrites upon cooling (Step 6).

As mentioned previously, the above-mentioned cracking mechanism stems from the liquid phase separation, which is due to the alloying elements with large positive enthalpy of mixing with Cu such as Cr, Fe and Mo. As these elements are widely utilized to improve corrosion resistance and mechanical properties, similar observations can be made for other Cu-Ni alloy combinations utilizing such elements. For example, phase separation and cracking were visible in OM images of L-PBF processed Cu-IN718 powder blends (IN718 contains Cr, Mo, and Fe) [14,15]. A similar behavior was apparent for L-PBF of CuSn10-IN718 in two different studies, where phase separation and cracks on the IN718 side of the interface were observed [19,20]. Another study investigating L-PBF of CuSn10-IN718 showed both phase separation and vertical cracks at the Ni-rich side of the interface [16]. Supporting the findings of this study, L-PBF of powder mixtures of CuSn10-IN718 led to extensive cracking for compositions 20 and 40 vol% CuSn10 [17]. However, cracking was also reported for 60 vol% CuSn10, which contrasts the cracking window in the current study. This can be explained by two considerations. First, the alloy systems, and thus, the corresponding solidification ranges are different, which may shift the cracking susceptibility window. Second, different powder mixtures with 20 vol% increments were printed on top of each other in the study, which leads to transition zones with compositions in-between. Conformingly, cracking is visible at the interface between 40 and 60 vol% CuSn10 mixtures, and it reduces progressively moving away from the interface towards higher CuSn10 compositions [17]. Hot tearing was also reported for the Cu8Cr4Nb-IN625 combination as well as liquid phase separation [18]. Both solidification cracking at Ni-rich compositions and cracking related to the formation of brittle intermetallics for Cu-rich compositions were observed for the Cu4Cr2Nb-IN625 combination [21,22]. Moreover, a recent study reported cracks for L-PBF of Cu15Ni8Sn and GH3230 (Ni-based alloy containing Cr, W and Fe), where Cu-rich and Ni-rich phases were also reported [76] On the other hand, compositionally graded interfaces without cracks were obtained during L-DED processing of Cu and Delero-22 Ni-based alloy, which contains only Si and B as alloying elements [13]. Since Si and B have negative enthalpies of mixing with liquid Cu [57], they do not cause immiscibility and further cracking. Therefore, these observations indicate that the proposed mechanism can be extended to cracking in Ni-Cu alloy combinations with alloying elements that have a positive enthalpy of mixing with Cu such as Cr, Co, Fe, Mo, V and W [57].

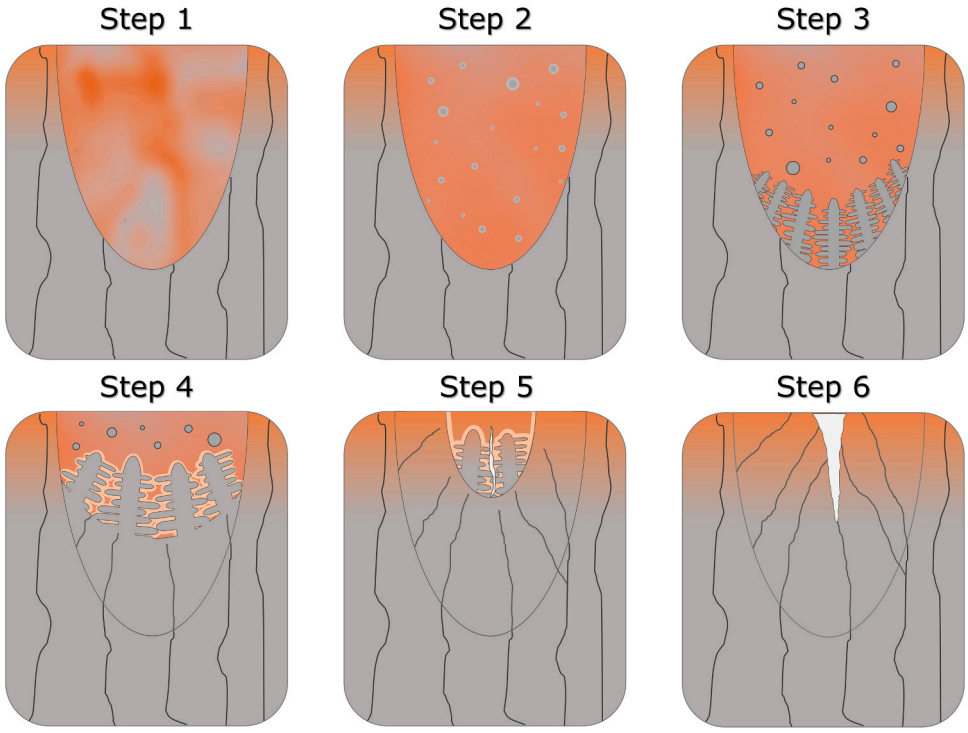

Fig. 10. Schematic representation of the cracking mechanism in Ni-Cu alloy systems. (1) Liquid mixing in the melt pool, (2) liquid phase separation, (3) competitive growth of Ni-rich cells/dendrites, (4) Cu-rich liquid segregation between the grain boundaries, (5) crack initiation at the grain boundaries, (6) crack propagation following the Cu-infiltrated centerline. The distorted black lines represent grain boundaries and the white regions represent the crack formed.

5. Conclusions

Processability of pure Ni and Cu is known to be excellent via fusion methods including welding, casting, and additive manufacturing owing to their complete solubility in liquid and solid state. However, during additive manufacturing of Ni-Cu alloy systems, cracking can be an important obstacle against producing sound parts. In order to understand the mechanism behind cracking in such multi-material parts, L-PBF of CuCrZr-IN625 alloy combinations were investigated using experimental and numerical approaches. The use of *operando* X-ray imaging and diffraction experiments performed with a miniature L-PBF system at synchrotron beamlines allowed to capture rapid transformations that occur during AM. Coupled with additional microstructure and composition characterization, this dual-pronged approach led to the drawing of a comprehensive picture of the cracking mechanism in Ni-Cu alloy combinations, as well as the dependance of cracking on processing conditions and composition. The following conclusions can be drawn based on these investigations:

- Cr, Fe, and Mo present in IN625 cause both liquid and solid immiscibility when mixed with CuCrZr due to the large positive enthalpy of mixing between Cu and these elements.
- Liquid phase separation takes place as a result of the miscibility gap, followed by the solidification of two distinct phases with significantly different freezing ranges. As a consequence, the mushy zone consisting of the Ni-rich solid and the Cu-rich liquid persists over a wide temperature range.
- The extended temperature range of solidification ultimately leads to solidification cracking at the grain boundaries due to liquid-solid phase formation shrinkage and thermal stresses generated during fast cooling from high temperature. The cracking occurs in the final stages of solidification, with cracks initiating from regions of Cu-rich liquid within the mushy zone.
- The most crack susceptible range of composition was identified to be 20–40 wt% CuCrZr-IN625 via thermodynamic calculations. Experimental validation through crack density measurements on the printed powder blends supported the calculated range of crack susceptibility.
- Different heat inputs lead to a shift in the composition of peak crack susceptibility, i.e., for a lower heat input, the crack susceptibility peaks at a higher CuCrZr amount. This shift was related to solute trapping and dendrite tip curvature undercooling experienced during rapid solidification, which alters the freezing range for a given composition.

Finally, as demonstrated by various examples in the literature exhibiting similar characteristics to those observed in this study, the proposed cracking mechanism may be applicable to other fusion processes utilizing Cu-Ni alloy combinations that incorporate elements known to promote liquid immiscibility with Cu, such as Cr, Co, Fe, Mo, V and W.

CRediT authorship contribution statement

Andaç Özsoy: Writing – original draft, Visualization, Validation, Methodology, Investigation, Formal analysis, Data curation, Conceptualization. **Steve Gaudez:** Writing – review & editing, Software, Methodology, Investigation, Conceptualization. **William A. Hearn:** Writing – review & editing, Methodology, Investigation, Conceptualization. **Antonios Baganis:** Visualization, Software, Formal analysis**. Zoltán Hegedüs:** Software, Resources, Formal analysis, Data curation. **Yunhui Chen:** Resources, Investigation, Data curation**. Alexander Rack:** Resources, Investigation, Data curation. **Roland E. Logé:** Writing – review & editing, Supervision, Resources. **Steven Van Petegem:** Writing – review & editing, Supervision, Resources, Project administration, Investigation, Funding acquisition, Data curation.

Funding

A.Ö. and S.V.P. acknowledge financial support by Board of the Swiss Federal Institutes of Technology (ETH Domain) within the SFA-AM MULTIMAT project. W.A.H. and S.V.P. thank Swiss National Science Foundation (SNSF) for financial support under grant agreement No 193799. This project has received funding from the European Union's Horizon Europe research and innovation program under the Marie Skłodowska-Curie Actions grant agreement No 884104. Y.C. acknowledges the support from the RMIT Vice Chancellor's Senior Research Fellowship. Y.C. acknowledges travel funding (AS/IA231/20264) provided by the International Synchrotron Access Program (ISAP) managed by the Australian Synchrotron, part of ANSTO, and funded by the Australian Government.

Declaration of Competing Interest

The authors declare that they have no known competing financial interests or personal relationships that could have appeared to influence the work reported in this paper.

Acknowledgments

We acknowledge the European Synchrotron Radiation Facility (ESRF) for provision of synchrotron radiation facilities under proposal numbers HC-5703 and MA-6233, and we would like to thank Jean Paul Valade and Diego Hopson Safatli for assistance and support in using beamline ID19. We acknowledge DESY (Hamburg, Germany), a member of the Helmholtz Association HGF, for the provision of experimental facilities. Parts of this research were carried out at PETRA III and we would like to thank Sven Gutschmidt for assistance in using P21.2. Beamtime was allocated for proposal I-20230515 EC.

Appendix A. Supporting information

Supplementary data associated with this article can be found in the online version at doi:10.1016/j.addma.2025.104950.

Data Availability

The data is openly available in https://zenodo.org/records/15413960

References

[1] B. Blakey-Milner, P. Gradl, G. Snedden, M. Brooks, J. Pitot, E. Lopez, M. Leary, F. Berto, A. du Plessis, Metal additive manufacturing in aerospace: a review, Mater. Des. 209 (2021) 110008, https://doi.org/10.1016/j.matdes.2021.110008.
[2] D. Wang, L. Liu, G. Deng, C. Deng, Y. Bai, Y. Yang, W. Wu, J. Chen, Y. Liu, Y. Wang, X. Lin, C. Han, Recent progress on additive manufacturing of multi-material structures with laser powder bed fusion, Virtual Phys. Prototyp. 17 (2022) 329–365, https://doi.org/10.1080/17452759.2022.2028343.
[3] A. Marques, B. Guimarães, M. Cerqueira, F. Silva, O. Carvalho, Multi-material inconel 718 parts with highly conductive copper cooling channels for aerospace applications, Adv. Eng. Mater. 25 (2023) 2201349, https://doi.org/10.1002/adem.202201349.
[4] S.A. Gavin, J. Billingham, J.P. Chubb, P. Hancock, Effect of trace impurities on hot ductility of as-cast cupronickel alloys, Met. Technol. 5 (1978) 397–401, https://doi.org/10.1179/mt.1978.5.1.397.
[5] S. Murphy, A. Ramchandani, R.L. Jones, P.C. Davies, Metallography and fracture toughness of conventional and Stir-Cast IN 768 cupronickel, Cast. Met 3 (1990) 68–72, https://doi.org/10.1080/09534962.1990.11819022.
[6] A.J. Fletcher, S. King, B. Rickinson, H. Atkinson, Effect of hot isostatic pressing on mechanical properties and microstructure of 70–30 cupronickel castings, Mater. Sci. Technol. 9 (1993) 555–561, https://doi.org/10.1179/mst.1993.9.7.555.
[7] G. Phanikumar, P. Dutta, K. Chattopadhyay, Continuous welding of Cu-Ni dissimilar couple using CO2 laser, Sci. Technol. Weld. Join. 10 (2005) 158–166, https://doi.org/10.1179/174329305X36043.
[8] W.-S. Chen, C.-Y. Wang, R.-K. Shiue, Brazing inconel 625 using the copper foil, Metall. Mater. Trans. A 44 (2013) 5724–5731, https://doi.org/10.1007/s11661-013-1954-x.

[9] L. Lin, W.U.H. Syed, A.J. Pinkerton, Rapid additive manufacturing of functionally graded structures using simultaneous wire and powder laser deposition, Virtual Phys. Prototyp. 1 (2006) 217–225, https://doi.org/10.1080/17452750601141523.

[10] S. Qu, S. Gao, L. Wang, J. Ding, Y. Lu, Y. Wen, X. Qu, B. Zhang, X. Song, Full-composition-gradient in-situ alloying of Cu–Ni through laser powder bed fusion, Addit. Manuf. 85 (2024) 104166, https://doi.org/10.1016/j.addma.2024.104166.

[11] Z. Liu, Q. Zhang, B. Zhang, Y. Wang, P. Zuo, Z. Zhang, J. Wu, X. Yan, Y. Huang, X. Li, Investigation on mechanical properties and corrosion behavior of laser powder bed fusion 70/30 copper-nickel alloy, Corros. Sci. 232 (2024) 112040, https://doi.org/10.1016/j.corsci.2024.112040.

[12] T. Pan, X. Zhang, T. Yamazaki, A. Sutton, W. Cui, L. Li, F. Liou, Characteristics of inconel 625—copper bimetallic structure fabricated by directed energy deposition, Int. J. Adv. Manuf. Technol. 109 (2020) 1261–1274, https://doi.org/10.1007/S00170-020-05713-Z.

[13] S. Karnati, Y. Zhang, F.F. Liou, J.W. Newkirk, On the feasibility of tailoring Copper–Nickel functionally graded materials fabricated through laser metal deposition, Metals 9 (2019), https://doi.org/10.3390/met9030287.

[14] A. El Hassanin, A.T. Silvestri, F. Napolitano, F. Scherillo, A. Caraviello, D. Borrelli, A. Astarita, Laser-powder bed fusion of pre-mixed Inconel718-Cu powders: an experimental study, J. Manuf. Process 71 (2021) 329–344, https://doi.org/10.1016/j.jmapro.2021.09.028.

[15] A.E.El Hassanin, A.T. Silvestri, F. Napolitano, A. Caraviello, D. Borrelli, A. Astarita, In situ alloying through Laser-Powder bed fusion of a 60%Inconel718-40%Cu powders mixture, Metallogr. Microstruct. Anal. 12 (2023) 413–426, https://doi.org/10.1007/s13632-023-00942-6.

[16] X. Yang, G. Zou, Z. Wang, X. He, M. Zhang, J. Xu, Interfacial characteristics and mechanical performance of IN718/CuSn10 fabricated by laser powder bed fusion, Crystals 15 (2025) 344, https://doi.org/10.3390/cryst15040344.

[17] G.-S. Zou, X. Yang, D.-X. Cheng, H. Gu, M.-N. Zhang, J.-Y. Xu, C. Wei, J.-H. Yao, L. Li, Interface characterization and mechanical properties of laser powder bed fused IN718-CuSn10 functionally gradient materials, Mater. Today Commun. 45 (2025) 112411, https://doi.org/10.1016/j.mtcomm.2025.112411.

[18] S.J. Hales, C.S. Domack, K.M. Taminger, Electron Beam Freeform Fabrication of Dissimilar Materials: Cracking in Inconel® 625 Deposited on GRCop-84, (2020) NASA/TP-2020-5005040.

[19] V. Nguyen, Functionally Magnetic Gradient Copper-nickel Material Fabricated Via Directed Energy Deposition, West Virginia University, 2022.

[20] L. Li, Q. Shi, S. Yang, In-situ bonding of horizontal bimetallic interface by laser offset during laser powder bed fusion of copper/nickel multi-material structures and underlying thermodynamic mechanisms, J. Mater. Process. Technol. 339 (2025) 118831, https://doi.org/10.1016/j.jmatprotec.2025.118831.

[21] J. Preis, D. Xu, B.K. Paul, P.A. Eschbach, S. Pasebani, Effect of liquid miscibility gap on defects in inconel 625–GRCop42 joints through analysis of gradient composition microstructure, J. Manuf. Mater. Process 8 (2024) 42, https://doi.org/10.3390/jmmp8010042.

[22] J. Preis, Z. Wang, J. Howard, Y. Lu, N. Wannenmacher, S. Shen, B.K. Paul, S. Pasebani, Effect of laser power and deposition sequence on microstructure of GRCop42 - inconel 625 joints fabricated using laser directed energy deposition, Mater. Des. 241 (2024) 112944, https://doi.org/10.1016/j.matdes.2024.112944.

[23] C. Ioannidou, H. König, N. Semjatov, U. Ackelid, P. Staron, C. Körner, P. Hedström, G. Lindwall, In-situ synchrotron X-ray analysis of metal additive manufacturing: current state, opportunities and challenges, Mater. Des. 219 (2022) 110790, https://doi.org/10.1016/j.matdes.2022.110790.

[24] S.M.H. Hojjatzadeh, Q. Guo, N.D. Parab, M. Qu, L.I. Escano, K. Fezzaa, W. Everhart, T. Sun, L. Chen, In-Situ characterization of pore formation dynamics in pulsed wave laser powder bed fusion, Materials 14 (2021) 2936, https://doi.org/10.3390/ma14112936.

[25] Z. Gan, O.L. Kafka, N. Parab, C. Zhao, L. Fang, O. Heinonen, T. Sun, W.K. Liu, Universal scaling laws of keyhole stability and porosity in 3D printing of metals, Nat. Commun. 12 (2021) 2379, https://doi.org/10.1038/s41467-021-22704-0.

[26] Y. Chen, S.J. Clark, C.L.A. Leung, L. Sinclair, S. Marussi, M.P. Olbinado, E. Boller, A. Rack, I. Todd, P.D. Lee, In-situ synchrotron imaging of keyhole mode multi-layer laser powder bed fusion additive manufacturing, Appl. Mater. Today 20 (2020) 100650, https://doi.org/10.1016/j.apmt.2020.100650.

[27] L. Sinclair, C.L.A. Leung, S. Marussi, S.J. Clark, Y. Chen, M.P. Olbinado, A. Rack, J. Gardy, G.J. Baxter, P.D. Lee, In situ radiographic and ex situ tomographic analysis of pore interactions during multilayer builds in laser powder bed fusion, Addit. Manuf. 36 (2020) 101512, https://doi.org/10.1016/j.addma.2020.101512.

[28] C. Zhao, K. Fezzaa, R.W. Cunningham, H. Wen, F. De Carlo, L. Chen, A.D. Rollett, T. Sun, Real-time monitoring of laser powder bed fusion process using high-speed X-ray imaging and diffraction, Sci. Rep. 2017 71 7 (2017) 1–11, https://doi.org/10.1038/s41598-017-03761-2.

[29] D.T. Rees, C. Lun Alex Leung, J. Elambasseril, S. Marussi, S. Shah, S. Marathe, M. Brandt, M. Easton, P.D. Lee, In situ X-ray imaging of hot cracking and porosity during LPBF of Al-2139 with TiB2 additions and varied process parameters, Mater. Des. 231 (2023) 112031, https://doi.org/10.1016/J.MATDES.2023.112031.

[30] H. Ghasemi-Tabasi, C. de Formanoir, S. Van Petegem, J. Jhabvala, S. Hocine, E. Boillat, N. Sohrabi, F. Marone, D. Grolimund, H. Van Swygenhoven, R.E. Logé, Direct observation of crack formation mechanisms with operando laser powder bed fusion X-ray imaging, Addit. Manuf. 51 (2022) 102619, https://doi.org/10.1016/J.ADDMA.2022.102619.

[31] N. Kouraytem, P.-J. Chiang, R. Jiang, C. Kantzos, J. Pauza, R. Cunningham, Z. Wu, G. Tang, N. Parab, C. Zhao, K. Fezzaa, T. Sun, A.D. Rollett, Solidification crack propagation and morphology dependence on processing parameters in AA6061 from ultra-high-speed x-ray visualization, Addit. Manuf. 42 (2021) 101959, https://doi.org/10.1016/j.addma.2021.101959.

[32] Y. Chen, S.J. Clark, D.M. Collins, S. Marussi, S.A. Hunt, D.M. Fenech, T. Connolley, R.C. Atwood, O.V. Magdysyuk, G.J. Baxter, M.A. Jones, C.L.A. Leung, P.D. Lee, Correlative synchrotron X-ray imaging and diffraction of directed energy deposition additive manufacturing, Acta Mater. 209 (2021) 116777, https://doi.org/10.1016/j.actamat.2021.116777.

[33] B. Wahlmann, E. Krohmer, C. Breuning, N. Schell, P. Staron, E. Uhlmann, C. Körner, In situ observation of γ′ phase transformation dynamics during selective laser melting of CMSX-4, Adv. Eng. Mater. 23 (2021) 2100112, https://doi.org/10.1002/ADEM.202100112.

[34] J. Epp, J. Dong, H. Meyer, A. Bohlen, Analysis of cyclic phase transformations during additive manufacturing of hardenable tool steel by in-situ X-ray diffraction experiments, Scr. Mater. 177 (2020) 27–31, https://doi.org/10.1016/J.SCRIPTAMAT.2019.09.021.

[35] S. Hocine, H. Van Swygenhoven, S. Van Petegem, C.S.T. Chang, T. Maimaitiyili, G. Tinti, D. Ferreira Sanchez, D. Grolimund, N. Casati, Operando X-ray diffraction during laser 3D printing, Mater. Today 34 (2020) 30–40, https://doi.org/10.1016/J.MATTOD.2019.10.001.

[36] V. Thampy, A.Y. Fong, N.P. Calta, J. Wang, A.A. Martin, P.J. Depond, A.M. Kiss, G. Guss, Q. Xing, R.T. Ott, A. van Buuren, M.F. Toney, J.N. Weker, M.J. Kramer, M. J. Matthews, C.J. Tassone, K.H. Stone, Subsurface cooling rates and microstructural response during laser based metal additive manufacturing, Sci. Rep. 2020 101 10 (2020) 1–9, https://doi.org/10.1038/s41598-020-58598-z.

[37] M. Chen, M. Simonelli, S. Van Petegem, Y. Yau Tse, C. Sin Ting Chang, M. Grazyna Makowska, D. Ferreira Sanchez, H. Moens-Van Swygenhoven, A quantitative study of thermal cycling along the build direction of Ti-6Al-4V produced by laser powder bed fusion, Mater. Des. 225 (2023) 111458, https://doi.org/10.1016/j.matdes.2022.111458.

[38] S. Gao, Z. Li, S. Van Petegem, J. Ge, S. Goel, J.V. Vas, V. Luzin, Z. Hu, H.L. Seet, D. F. Sanchez, H. Van Swygenhoven, H. Gao, M. Seita, Additive manufacturing of alloys with programmable microstructure and properties, Nat. Commun. 14 (2023) 6752, https://doi.org/10.1038/s41467-023-42326-y.

[39] M. Hamidi Nasab, G. Masinelli, C. de Formanoir, L. Schlenger, S. Van Petegem, R. Esmaeilzadeh, K. Wasmer, A. Ganvir, A. Salminen, F. Aymanns, F. Marone, V. Pandiyan, S. Goel, R.E. Logé, Harmonizing sound and light: X-ray imaging unveils acoustic signatures of stochastic inter-regime instabilities during laser melting, Nat. Commun. 14 (2023) 8008, https://doi.org/10.1038/s41467-023-43371-3.

[40] V. Pandiyan, G. Masinelli, N. Claire, T. Le-Quang, M. Hamidi-Nasab, C. de Formanoir, R. Esmaeilzadeh, S. Goel, F. Marone, R. Logé, S. Van Petegem, K. Wasmer, Deep learning-based monitoring of laser powder bed fusion process on variable time-scales using heterogeneous sensing and *operando* X-ray radiography guidance, Addit. Manuf. 58 (2022) 103007, https://doi.org/10.1016/j.addma.2022.103007.

[41] S. Hocine, H. Van Swygenhoven, S. Van Petegem, Verification of selective laser melting heat source models with operando X-ray diffraction data, Addit. Manuf. 37 (2021) 101747, https://doi.org/10.1016/j.addma.2020.101747.

[42] S. Hocine, S. Van Petegem, U. Frommherz, G. Tinti, N. Casati, D. Grolimund, H. Van Swygenhoven, A miniaturized selective laser melting device for operando X-ray diffraction studies, Addit. Manuf. 34 (2020) 101194, https://doi.org/10.1016/J.ADDMA.2020.101194.

[43] Z. Hu, B. Gan, J. Tan, J. Wu, S. Chen, J. Dong, Z. Ma, The enhancement of laser absorptivity and properties in laser powder bed fusion manufactured Cu-Cr-Zr alloy by employing Y2O3 coated powder as precursor, J. Alloy. Compd. 927 (2022) 167111, https://doi.org/10.1016/j.jallcom.2022.167111.

[44] Y. Qin, B. Wu, G. Wang, P. Song, D.J. Förster, M. Huang, S. Yang, Light absorption of W-Cu powders in laser powder bed fusion, Opt. Laser Technol. 162 (2023) 109243, https://doi.org/10.1016/j.optlastec.2023.109243.

[45] P.G. Klemens, T.K. Chu, Thermal Conductivity 14, Springer US, Boston, MA, 1976, https://doi.org/10.1007/978-1-4899-3751-3.

[46] S.A. Hosseini, A. Abdollah-zadeh, H. Naffakh-Moosavy, A. Mehri, Elimination of hot cracking in the electron beam welding of AA2024-T351 by controlling the welding speed and heat input, J. Manuf. Process 46 (2019) 147–158, https://doi.org/10.1016/j.jmapro.2019.09.003.

[47] B. Kumar, S. Sahu, D. Srinivasan, B.N. Jaya, Influence of heat input on solidification cracking in additively manufactured CM247LC Ni-based superalloy, Metall. Mater. Trans. A 54 (2023) 2394–2409, https://doi.org/10.1007/s11661-023-07027-7.

[48] Z. Ren, D.Z. Zhang, G. Fu, J. Jiang, M. Zhao, High-fidelity modelling of selective laser melting copper alloy: laser reflection behavior and thermal-fluid dynamics, Mater. Des. 207 (2021) 109857, https://doi.org/10.1016/j.matdes.2021.109857.

[49] G. Ashiotis, A. Deschildre, Z. Nawaz, J.P. Wright, D. Karkoulis, F.E. Picca, J. Kieffer, The fast azimuthal integration python library: pyFAI, J. Appl. Crystallogr 48 (2015) 510–519, https://doi.org/10.1107/S1600576715004306.

[50] J. Schindelin, I. Arganda-Carreras, E. Frise, V. Kaynig, M. Longair, T. Pietzsch, S. Preibisch, C. Rueden, S. Saalfeld, B. Schmid, J.-Y. Tinevez, D.J. White, V. Hartenstein, K. Eliceiri, P. Tomancak, A. Cardona, Fiji: an open-source platform for biological-image analysis, Nat. Methods 9 (2012) 676–682, https://doi.org/10.1038/nmeth.2019.

[51] J.-O. Andersson, T. Helander, L. Höglund, P. Shi, B. Sundman, Thermo-Calc & DICTRA, computational tools for materials science, Calphad 26 (2002) 273–312, https://doi.org/10.1016/S0364-5916(02)00037-8.

[52] S. Kou, A criterion for cracking during solidification, Acta Mater. 88 (2015) 366–374, https://doi.org/10.1016/j.actamat.2015.01.034.

[53] J. Liu, S. Kou, Effect of diffusion on susceptibility to cracking during solidification, Acta Mater. 100 (2015) 359–368, https://doi.org/10.1016/j.actamat.2015.08.064.

[54] J. Liu, H.P. Duarte, S. Kou, Evidence of back diffusion reducing cracking during solidification, Acta Mater. 122 (2017) 47–59, https://doi.org/10.1016/j.actamat.2016.09.037.
[55] S. Kou, Predicting susceptibility to solidification cracking and liquation cracking by CALPHAD, Metals 11 (2021) 1442, https://doi.org/10.3390/met11091442.
[56] Practice for Determining Average Grain Size Using Electron Backscatter Diffraction (EBSD) in Fully Recrystallized Polycrystalline Materials, (n.d.). https://doi.org/10.1520/E2627-13.
[57] A. Takeuchi, A. Inoue, Mixing enthalpy of liquid phase calculated by miedema's scheme and approximated with sub-regular solution model for assessing forming ability of amorphous and glassy alloys, Intermetallics 18 (2010) 1779–1789, https://doi.org/10.1016/j.intermet.2010.06.003.
[58] A. Verma, J.B. Singh, S.D. Kaushik, V. Siruguri, Lattice parameter variation and its effect on precipitation behaviour of ordered Ni2(Cr,Mo) phase in Ni-Cr-Mo alloys, J. Alloy. Compd. 813 (2020) 152195, https://doi.org/10.1016/j.jallcom.2019.152195.
[59] A. Mostafaei, R. Ghiaasiaan, I.-T. Ho, S. Strayer, K.-C. Chang, N. Shamsaei, S. Shao, S. Paul, A.-C. Yeh, S. Tin, A.C. To, Additive manufacturing of nickel-based superalloys: a state-of-the-art review on process-structure-defect-property relationship, Prog. Mater. Sci. 136 (2023) 101108, https://doi.org/10.1016/j.pmatsci.2023.101108.
[60] T.B. Massalski, J.L. Murray, L.H. Bennet, Binary alloy phase diagrams: Volume 1, in: ASM Int., 1986: p. 1100. https://doi.org/10.31399/asm.hb.v03.a0006247.
[61] Y.K. Zhang, J. Gao, L.L. Wei, M. Kolbe, T. Volkmann, D. Herlach, Novel insight into microstructural evolution of phase-separated Cu–Co alloys under influence of forced convection, J. Mater. Sci. 46 (2011) 6603–6608, https://doi.org/10.1007/s10853-011-5609-2.
[62] J. Zhang, X. Cui, Y. Wang, Liquid phase separation in immiscible Cu–Fe alloys, Int. J. Cast. Met. Res. 31 (2018) 87–92, https://doi.org/10.1080/13640461.2017.1367527.
[63] H.H. König, N.H. Pettersson, A. Durga, S. Van Petegem, D. Grolimund, A. C. Chuang, Q. Guo, L. Chen, C. Oikonomou, F. Zhang, G. Lindwall, Solidification modes during additive manufacturing of steel revealed by high-speed X-ray diffraction, Acta Mater. 246 (2023) 118713, https://doi.org/10.1016/J.ACTAMAT.2023.118713.
[64] S. Dasgupta, S. Kou, Undercooling and cracking during solidification, Metall. Mater. Trans. A (2024), https://doi.org/10.1007/s11661-024-07486-6.
[65] P. Scheel, P. Markovic, S. Van Petegem, M.G. Makowska, R. Wrobel, T. Mayer, C. Leinenbach, E. Mazza, E. Hosseini, A close look at temperature profiles during laser powder bed fusion using operando X-ray diffraction and finite element simulations, Addit. Manuf. Lett. 6 (2023) 100150, https://doi.org/10.1016/j.addlet.2023.100150.
[66] L. Liu, D. Wang, G. Deng, Z. Liu, C. Tan, X. Zhou, C. Han, R. Jiang, Y. Yang, Crack inhibition to enhance strength-ductility of CM247LC alloy fabricated by laser powder bed fusion, Mater. Sci. Eng. A 875 (2023) 145114, https://doi.org/10.1016/j.msea.2023.145114.
[67] H. Javidrad, B. Koc, Study of the Effect of Process Parameters and Heat Treatment on the Formation and Evolution of Directed Energy Deposition of IN718-CuCrZr Interface, Adv. Eng. Mater. n/a (n.d.) 2500773. https://doi.org/10.1002/adem.202500773.
[68] D. Yuan, X. Sun, J. Wang, Z. Zhang, D. Cheng, C. Wei, L. Li, Cracking behavior of IN718/Cu10Sn bimetallic structures fabricated by laser directed energy deposition with different deposition sequences, J. Alloy. Compd. 1033 (2025) 181222, https://doi.org/10.1016/j.jallcom.2025.181222.
[69] L. Zhang, P. Dong, Y. Zeng, H. Yao, J. Chen, Additive manufacturing of inconel 718/CuCrZr multi-metallic materials fabricated by laser powder bed fusion, Addit. Manuf. 92 (2024) 104377, https://doi.org/10.1016/j.addma.2024.104377.
[70] B. Zhang, H. Xiao, Z. Gao, Y. Li, W. Zhang, G. Zhou, H. Zhu, Process optimization and characterization of Inconel718 coatings on high copper alloys by laser-based directed energy deposition, Prog. Addit. Manuf. (2025), https://doi.org/10.1007/s40964-025-01196-0.
[71] Y. Bai, J. Zhang, C. Zhao, C. Li, H. Wang, Dual interfacial characterization and property in multi-material selective laser melting of 316L stainless steel and C52400 copper alloy, Mater. Charact. 167 (2020) 110489, https://doi.org/10.1016/j.matchar.2020.110489.
[72] A. Bulloch, A. Harris, A. Groom, A. Cruchley, C.J. Tuck, M. Simonelli, Fundamental investigation of the interface formation of Multi-material additive manufactured 316L-CuSn10 structures, Metall. Mater. Trans. A (2025), https://doi.org/10.1007/s11661-025-07817-1.
[73] C.P. Martendal, P.D.B. Esteves, L. Deillon, F. Malamud, A.M. Jamili, J.F. Löffler, M. Bambach, Effects of beam shaping on copper-steel interfaces in multi-material laser beam powder bed fusion, J. Mater. Process. Technol. 327 (2024) 118344, https://doi.org/10.1016/j.jmatprotec.2024.118344.
[74] T. Schroeder, M. Lehmann, M. Horn, P. Kindermann, I. Uensal, F. Michal, A. Lippus, G. Schlick, C. Seidel, Transition zone parameter development in multi-material powder bed fusion: a general approach, Prog. Addit. Manuf. 9 (2024) 613–624, https://doi.org/10.1007/s40964-024-00663-4.
[75] C. Zhu, Z. Tang, A. Wang, J. Mu, P. Ren, Y. Wu, T. Sun, J. Zheng, H. Wang, H. Wang, Achieving ultra-high efficiency in directed energy deposition of pure copper on inconel 718 substrate with a 3500 w blue laser, Mater. Lett. 372 (2024) 137082, https://doi.org/10.1016/j.matlet.2024.137082.
[76] J. Gao, Q. Han, S. Soe, L. Wang, Z. Zhang, H. Zhang, J. Song, Y. Liu, R. Setchi, S. Yang, Laser additive manufacturing of TiB2-modified Cu15Ni8Sn/GH3230 heterogeneous materials: processability, interfacial microstructure and mechanical performance, Mater. Sci. Eng. A 900 (2024) 146496, https://doi.org/10.1016/j.msea.2024.146496.